Mapping glacier structure in inaccessible areas from turning seismic sources into a dense seismic array

Ugo Nanni[1], Philippe Roux[2], Florent Gimbert[3]

[1]Department of Geosciences, University of Oslo, Oslo, Norway
[2]Université Grenoble Alpes, CNRS, ISTerre, 38000 Grenoble, France
[3]Université Grenoble Alpes, CNRS, IRD, Grenoble INP, IGE, Grenoble, France

Key Points:

- We transform seismic sources from crevasses into virtual receivers using source-to-receiver spatial reciprocity
- We derive phase velocity maps in previously inaccessible areas with a resolution five times larger than traditional approaches
- We retrieve the influence of glacier geometry and structural heterogeneity on the glacier mechanical properties

Corresponding author: Ugo Nanni, `nanni@uio.no`

Abstract

Understanding glaciers structural heterogeneity is crucial for assessing their fate. Yet, places where structure changes are strong, such as crevasses fields, are often inaccessible for direct instrumentation. To overcome this limitation, we introduce an innovative technique that transforms seismic sources, here generated by crevasses, into virtual receivers using source-to-receiver spatial reciprocity. We demonstrate that phase interference patterns between well-localized seismic sources can be leveraged to retrieve phase velocity maps using Seismic Michelson Interferometry. The obtained phase velocity exhibits sensitivity to changes in glacier structure, offering insights into the origins of mechanical property changes, with spatial resolution surpassing traditional methods by a factor of five. In particular, we observe sharp variations in phase velocity related to strongly-damaged subsurface areas indicating a complex 3-D medium. Applying this method more systematically and in other contexts will enhance our understanding of the structure of glaciers and other seismogenic environments.

Plain Language Summary

1 Introduction

Monitoring structural heterogeneities of materials is crucial for assessing their mechanical behavior, ranging from biological tissues like bones (Hernigou, 2022) to geological formations such as rocks (Pyrak-Nolte et al., 2005), landslides (Chmiel, Walter, et al., 2021), earthquakes (Marty et al., 2019), and glaciers (Nanni et al., 2022). In the context of ice shelves and glaciers, mechanical heterogeneity, particularly manifested through crevasses, plays a key role in preconditioning disintegration and influencing ice flow (e.g., Pine Island, Thwaites ice shelves, Marmolada glacier; Lhermitte et al., 2020; Taylor et al., 2023).

Crevasses, which primarily form near the surface under extensive stress regimes (Van der Veen, 1998), exhibit a wide range of depths, from a few tens of meters if air-filled (Schuster & Rigsby, 1954) to the full glacier thickness if water-filled (Chandler & Hubbard, 2023). Crevasses facilitate the routing of surface meltwater to the sub-glacial environment, significantly modifying the ice-bed mechanical coupling and glacier thermal regime (Gagliardini & Werder, 2018; Gilbert et al., 2020).

Probing the impact of such heterogeneities on the mechanical properties of the medium is, however, challenging due to limited in-situ sampling possibilities. Consequently, remote sensing techniques, particularly passive seismic methods, are often employed to investigate mechanical heterogeneity. Passive seismic techniques traditionally consist in tracking the spatial coherence of the continuously-recorded seismic wavefield (noise) through an array of sensors (e.g., Shapiro et al., 2005; Curtis et al., 2006; Xu et al., 2012; Share et al., 2019). Applications of these techniques on glaciers include monitoring temporal changes in ice masses (Mordret et al., 2016), changes at the ice-bed interface (Zhan, 2019) and spatial changes in ice thickness (Sergeant et al., 2020).

One challenge with using noise sources is ensuring azimuthal equipartitioning of sources (Lobkis & Weaver, 2001; Fichtner et al., 2019). Recent studies have adopted a different approach with impulsive sources of known positions (Walter et al., 2015; Gimbert, Nanni, et al., 2021). In Gimbert, Nanni, et al. (2021) these sources were located using automatic Matched Field Processing (MFP) on continuous seismic records from an Alpine glacier. Analyzing these sources through Rayleigh surface wave travel-time-delays tomography (font map; Fig. 1) revealed, at first order, a non-unique relationship between crevasse occurrence and seismic phase velocities, offering insights into the glacier structure. Locations with higher crevasse occurrence were generally associated with lower phase velocities (< 1550 m.s^{-1}, southwest glacier flank; Fig. 1). This observation was however not systematic, since higher velocities (> 1630 m.s^{-1}) were also observed where

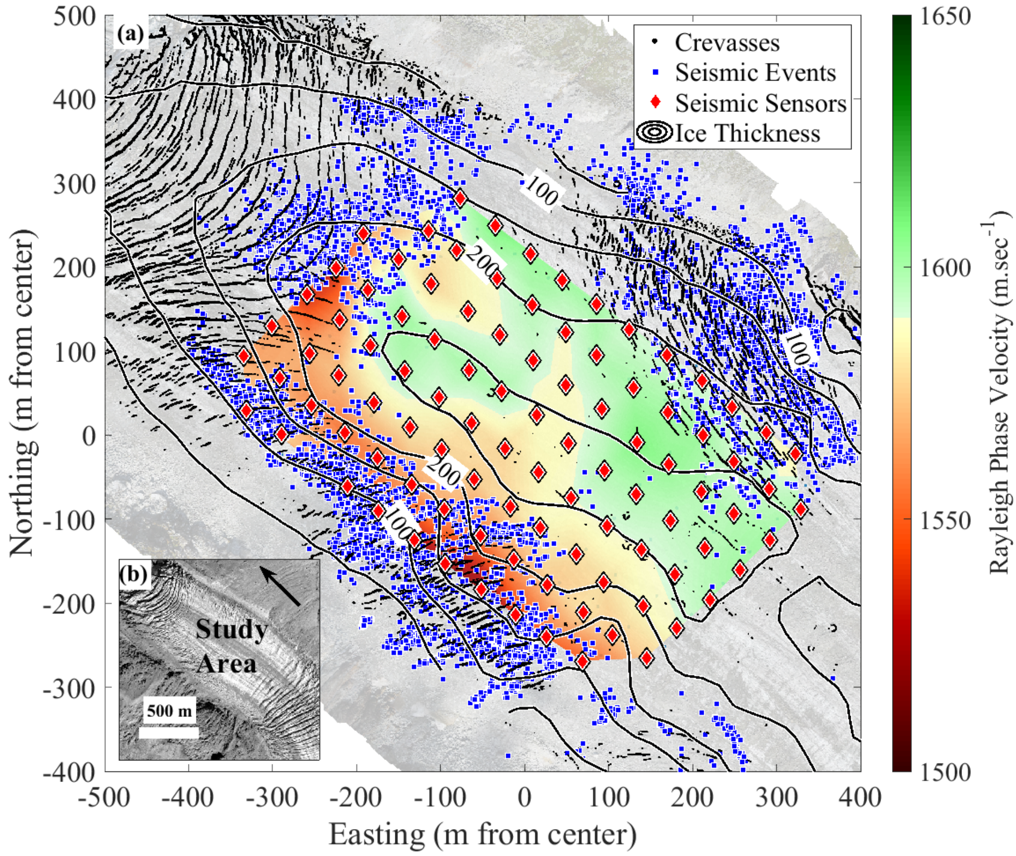

Figure 1. (a) Monitoring set-up on the Glacier d'Argentière. Red diamonds show the 98 seismic sensors. Black lines show 50 m-spaced ice thickness contours. Square blue dots show the seismic events location. Colored area shows phase velocities from Rayleigh-wave travel-time tomography at 13 Hz as in Figure 8 in Gimbert, Nanni, et al. (2021). Crevasses location (black) is shown on the background. Glacier flows toward northwest (black arrow in (b)). (b) Aerial view provided by Bruno Jourdain. The study area is located at c. 2400m of elevation and at 45°57'80"N 6°58'43"E.

crevasses are also present (northeast glacier flank; Fig. 1). This complexity highlights how phase velocity may also be influenced by other parameters such as ice thickness and micro-structure. Obtaining conclusive results regarding the effect of structural heterogeneity on glacier seismic structure is thus hindered by the difficulty of sampling the wavefield outside of areas where instrumentation is possible.

Here, we introduce an innovative technique that utilizes source-to-receiver spatial reciprocity (Knopoff & Gangi, 1959) to transform impulsive seismic sources into virtual receivers. This approach enables direct sampling of the wavefield within otherwise inaccessible areas. We demonstrate that phase interference patterns (Curtis, 2009) between well-localized seismic events can be leveraged to retrieve phase velocity maps at an unprecedented spatial resolution. Our method gives access to previously unreachable seismogenic regions, akin to deploying a dense seismic array within such areas.

2 Data and Methods

2.1 Data and Study area

We use a catalog of seismic events collected within the framework of the RESOLVE project (Gimbert, Nanni, et al., 2021) in the ablation zone of the Argentière Glacier in the French Alps. The catalog was obtained from an array of 98 3-component geophones (Fairfield Nodal Z-Land) deployed over an area of 650 m x 800 m, with a 40 to 50 m station-interspacing (red diamonds; Fig. 1). Continuous acquisitions were conducted over a 35-day period during the onset of the 2018 melt season, from April to June. The glacier thickness at the array location varies from 100 to 260 m (black lines; Fig. 1), and the glacier flow surface velocity reached 80 m.yr^{-1} during the study period (Gimbert, Nanni, et al., 2021).

The catalog encompasses 10,514 seismic events (blue squares; Fig. 1) localized with MFP at 11 ± 2 Hz and compiled by Gimbert, Nanni, et al. (2021) and Nanni et al. (2022). For each source, the MFP yields an optimized (x, y, z) location together with a phase velocity optimized over all source-to-receiver paths . This catalog offers a meter-scale resolution on the (x, y) plane (0.7–1 MFP output range; Nanni et al., 2022). We select seismic sources located near the glacier surface, within 400 m from the array center. The event are pulses (< 1sec) of similar waveforms propagating through the entire array with a predominant contribution from Rayleigh waves (Fig. S1) and are best described by a point-source mechanism (Eq. 2 in Nanni et al., 2022).

2.2 Methods

2.2.1 Waveform synchronization

At each receiver (geophone) we synchronize all 10,514 waveforms. For each event (Fig. S1a) we subtract the source-receiver propagation time based on the source-receiver distance and the associated phase velocity. We average these synchronized waveforms over the 98 receivers and cross-correlate this averaged waveform to each of the 98 waveforms to obtain an absolute origin time t_0. Finally, we subtract t_0 to each of the 10,514 waveforms throughout the receiver array and obtain, for each receiver, a synchronized dataset (Fig. S1b) with a time accuracy of 5 ms (Nyquist criteria given a 400 Hz sampling rate).

2.2.2 Surface Wave Diffraction Kernels

In order to retrieve phase velocity maps at the location of the seismic sources, we first construct Diffraction Kernels (DKs). DKs emerge from interference patterns between two wavefields and are dominated by surface waves (Walker, 2012; Fichtner et al., 2016). DKs are highly sensitive to the velocity structure as they carry phase information related to the diffraction of seismic waves from small-scale features in the medium. DKs are entirely data-based so no model calculation are needed. We compute the DKs using both convolution-based interferometry $\mathrm{DK_{conv}}$ and correlation-based interferometry $\mathrm{DK_{corr}}$ (Eqs. 3 and 4 in Chmiel et al., 2018). Considering a 2D-space geometry, pairs of receivers in r_1 and r_2, and a set of sources s (in r_s), $\mathrm{DK_{conv}}$ and $\mathrm{DK_{corr}}$ are defined as:

$$\mathrm{DK_{conv}}(\omega; r_s, r_1, r_2) = G(\omega; r_s, r_1)G(\omega; r_s, r_2) \tag{1}$$

$$\mathrm{DK_{corr}}(\omega; r_s, r_1, r_2) = G(\omega; r_s, r_1)G^*(\omega; r_s, r_2), \tag{2}$$

where $G(\omega; r_s, r_1)$ is the Fourier transform of the recorded signal at angular frequency ω and $*$ expresses the conjugate operation. $\mathrm{DK_{corr}}$ are derived from phase differences while $\mathrm{DK_{conv}}$ rely on phase additions. $\mathrm{DK_{conv}}$ necessitates the synchronization of sources with receivers.

We focus here on the phase variations, so amplitude-related issues associated with the physical coupling of receivers and sources to the medium cancel out. This emphasis on phase underscores the dominant role played by local velocity variations, aligning with the primary objective of surface wave tomography. However, it restricts the exploration of local attenuation, which, given our near-field configuration (investigated wavelength of ~ 150 m and array geometry of $\sim 400\times400$ m), can be considered a second-order effect.

Following the reciprocity principle (Knopoff & Gangi, 1959), the roles of sources and receivers can be physically interchanged. This reciprocity implies that a geophone can be considered either a source or a receiver, and the same applies to an icequake. Consequently, the spatial sampling of the DKs depends on the distribution of icequakes (10,514 points) and is no longer constrained by the spatial sampling of the geophone (98 points). This is where stands the key difference with classical surface-wave tomography approach where the spatial resolution and extent of the tomographic image is solely defined by the geophone array.

2.2.3 Seismic Michelson Interferometry

After computing the DKs, we image the medium using an iterative inversion scheme based on the Seismic Michelson Interferometry (SMI). This method has been applied successfully on empirical and synthetic datasets to retrieve phase velocity spatial variations (Chmiel et al., 2018; Chmiel, Roux, et al., 2021). The objective of SMI is to generate a high-resolution image of the subsurface by projecting the observed seismic interference patterns, DKs, on a modeled phase-velocity space F. Similar to optical interferometry and Eikonal tomography (Lin et al., 2009), SMI accounts for bent rays and operates without the need for travel-time measurements. Moreover, SMI is a data-driven inversion technique distinct from Full Waveform Inversion-based methods (Métivier et al., 2013).

The first step is an iterative tomographic inversion at a given pair of receiver and over all sources. We model theoretical phase-dependent interference patterns (Eqs. 6 and 7 in Chmiel et al., 2018) for a given receiver pair r_1 and r_2 and a source position r_s as:

$$F_{\text{conv}}(\omega; r_s, r_1, r_2; c) = \exp(\frac{i\omega}{c}(\|r_s - r_1\| + \|r_s - r_2\ \|), \tag{3}$$

$$F_{\text{corr}}(\omega; r_s, r_1, r_2; c) = \exp(\frac{i\omega}{c}(\|r_s - r_1\| - \|r_s - r_2\ \|). \tag{4}$$

The single-frequency diffraction formulation places local constraint on the phase velocity c at the location of the receiver pair and the source. Similarly to Eikonal tomography (Lin et al., 2009) and in contrast with Rayleigh-wave travel-time tomography (Fig.1), this means that the obtained phase velocities are independent of the source-receiver paths (Virieux et al., 2017; Chmiel, Roux, et al., 2021).

Then, we iteratively match the data-based DKs to the synthetic F to optimize the local phase velocity. We define a least-squares misfit function as:

$$\|F_{\text{conv}} - \text{DK}_{\text{conv}}\|^2 + \|F_{\text{corr}} - \text{DK}_{\text{corr}}\|^2, \tag{5}$$

with an initial phase velocity of the medium of 1589 m.s^{-1} (i.e., mean of the MFP-optimized velocities; Nanni et al., 2022). At each iteration we minimize Eq. 5 using a gradient-based optimization and from the local residual we update the phase velocity at each source (Eqs. 5 and 6 in Chmiel, Roux, et al., 2021). The iteration process stops when the normalized misfit reaches less than 4%. At a given source, this means that the local phase difference between the observed DKs and the synthetic F is turned iteratively into a local phase velocity, making the results independent across neighboring events. The iterations permit to avoid cycle skipping issues that could arise from phase differences that are too strong. The joint inversion of DK_{conv} and DK_{corr} allows to optimize the balance between resolution and robustness (Fig. 9 in Chmiel et al., 2018).

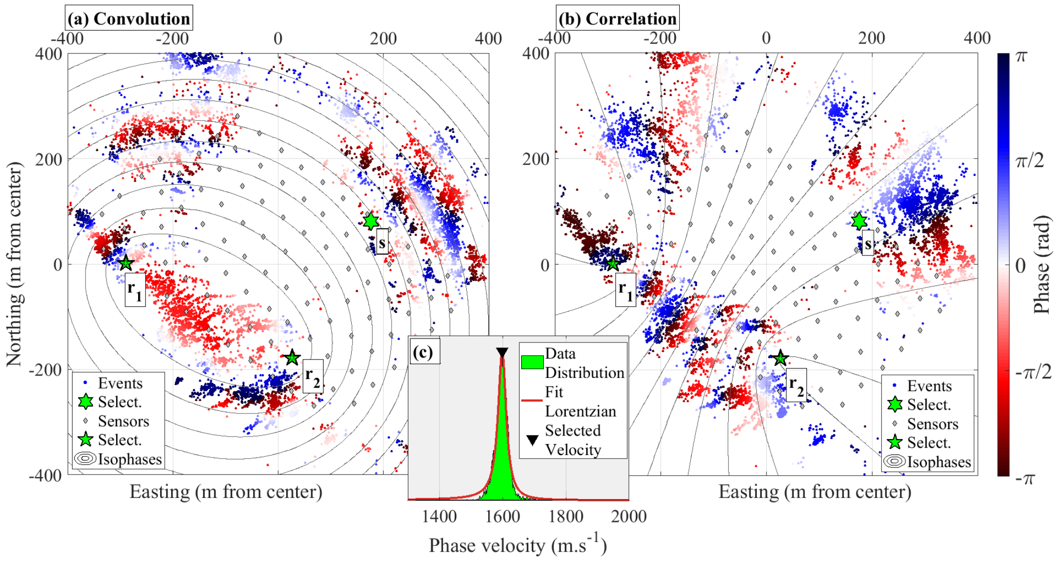

Figure 2. Phase patterns of the Data-based Diffraction Kernels (DKs) obtained at 11 ± 2 Hz from (a) convolution-based and (b) correlation-based interferometry between two receivers of the array in r_1 and r_2 (green pentagrams) and displayed at each icequake location. Contour lines show where the theoretical isophases switch sign, i.e. at $[-\pi, 0, \pi]$ (Eqs.3, 4 ; Fig. S2). (c, lower panel) distribution of local phase velocities (green) obtained at a given icequake location (shown in s, green hexagram) for all receiver pairs. A Cauchy-Lorentz distribution is fitted on the data (red line).

Finally, we perform the inversion for each of the 4,753 receiver pairs ($\frac{N_{\text{receiver}} \times (N_{\text{receiver}}-1)}{2}$) and obtain for each source a local phase velocity distribution (Fig. 2c). We define the local velocity at a given source as the peak value of the distribution and define the associated uncertainty as the standard deviation of the distribution. We note that the value of the standard deviation represents the measurement error, but also includes the spatial variability of the phase velocity inside the array (Fig.1) as well as potential anisotropy effects (Sergeant et al., 2020). As the phase velocity results from a statistical ensemble average over all DKs, and since source location uncertainties are independent from one source to another (Nanni et al., 2022), the single source location uncertainty is diluted in the statistics, broadening the distribution. Finally, as we solely depend on surface wave issued from icequakes located close to the glacier surface (within one wavelength) and given that there is no trade-off between (x, y) and (z) source localization (Nanni et al., 2022), the source depth uncertainty is expected to have no effect in our analysis.

3 Results

In Figure 2a, b (blue to red fringes), we present the data-based Diffraction Kernels (DKs) acquired at 11 ± 2 Hz at one receiver pair from the 10,514 sources. Over the study area, we observe alternating phase values manifested as diffraction 'fringes' in both $\mathrm{DK}_{\mathrm{conv}}$ and $\mathrm{DK}_{\mathrm{corr}}$. These fringes, reminiscent of classical Michelson fringes in optics (Shankland, 1974), underscore the coherence of the wavefield. The $\mathrm{DK}_{\mathrm{conv}}$ (Fig. 2a) exhibits an elliptical shape with a primary area of influence being located between the two receivers. This alignment is expected from sensitivity kernels for surface waves and provide information about the extent of the Fresnel zones (i.e., the region of constructive

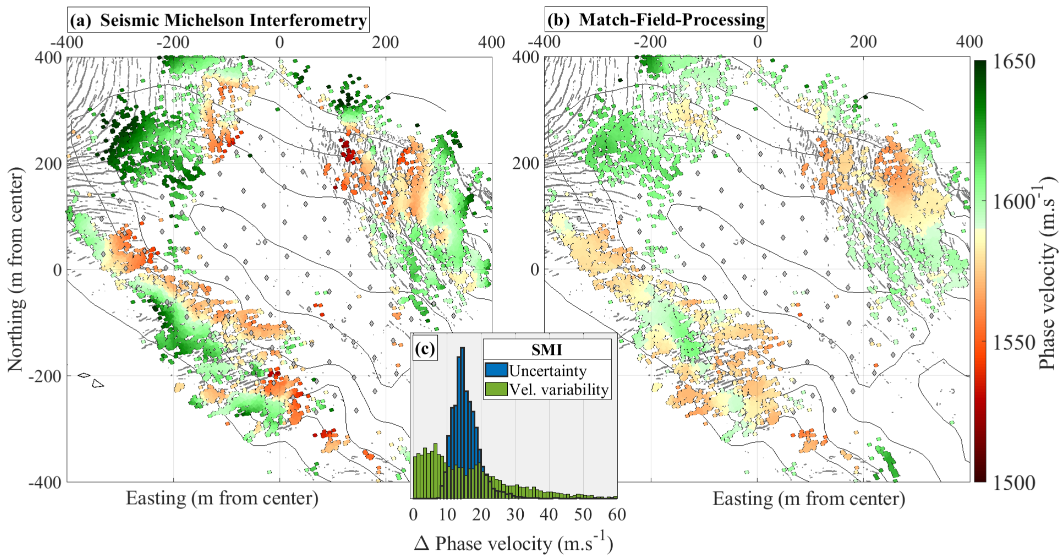

Figure 3. Phase velocity map at 11 ± 2 Hz obtained (a) from Seismic Michelson Interferometry (SMI) and (b) from Match Field Processing (MFP). Black lines show ice thickness contours and diamond markers show geophones location. Crevasses location is shown on the background. (c) Distribution of the SMI-phase velocity variability (green) and of the SMI-phase velocity uncertainty (blue).

interference Guest & Clouston, 1950; Yoshizawa & Kennett, 2002). Conversely, the DK_{corr} (Fig. 2b) presents a hyperbolic shape with phase oscillations linked to the stationary-phase area aligned with the two receivers (Snieder, 2004; Roux et al., 2004; Walker, 2012; Fichtner et al., 2016). Alongside the observed phase variations, we show contour lines (black lines in Fig. 2a, b) associated with the theoretical iso-phase computed from Eqs. 1 and 2 for a uniform velocity (Fig. S2 for the full phase pattern). The alignment between the DKs and the theoretical iso-phase highlights the suitability of our phase velocity optimization (Eq. 5). Additionally, we observe that the spatial distribution of sources is dense enough to avoid spatial aliasing in sampling of the DKs. Finally, the rapid spatial fluctuations observed between neighboring sources underscore the limited influence of the receiver-array geometry as well as the importance of having a large number of well-localized sources.

In Figure 2c, we present the phase velocity distribution obtained for one source (s, green hexagram in Fig. 2a, b). The distribution is optimally fitted by a Lorentzian function, from which we take the maximum as the local phase velocity. Such a narrow distribution, compared to a Gaussian distribution as in Chmiel, Roux, et al. (2021), underscores the accuracy of our results, marking a departure from conventional methods and reassessing the robustness of local phase velocity determination.

In Figure 3a, b, we present the phase velocities at 11 ± 2 Hz obtained from Seismic Michelson Interferometry (SMI) and from Matched Field Processing (MFP). For the SMI map (Fig. 3a) we show, at each source location, the peak of the local phase velocity distribution obtained from the collection of 4,753 convolution and correlation DKs as illustrated in Figure 2c. For the MFP map (Fig. 3b) we show at each source location, the phase velocity optimized in the MFP process (Nanni et al., 2022). While the SMI velocities are obtained with local constraints (Eqs. 3 and 4), the MFP velocities represent the medium's phase velocities as averaged over all source-to-station paths. At first order, and especially near the glacier flanks, the two methods exhibit similar characteristics to the previous surface wave inversions conducted on the receiver array through travel-time tomography (Fig. 1; Fig. S3). At finer spatial scale, and especially in the northern part of the array, we observe local discrepancies between the travel-time tomography-based velocity field and the SMI-based velocity field (Fig. 3; Fig. S3). Such discrepancies occur over small spatial scales ($<$ 50 m) and are likely related to the different spatial resolutions associated with the two velocity maps. Comparing the SMI and MFP maps reveals analogous spatial heterogeneities centering around the expected value for ice phase velocity ($\sim$ 1580 m.s^{-1} at 11 Hz; Gimbert, Nanni, et al., 2021), with SMI-inverted velocities of 1594 $\pm$ 21 m.s^{-1} and MFP-inverted velocities of 1589$\pm$ 12 m.s^{-1}. Nevertheless, SMI-inverted velocities reveal faster changes (higher spatial resolution) and sharper contrasts (a larger range of velocities) in the phase velocity field. The higher spatial resolution is likely related to the dense spatial distribution of icequakes, which provide more 'sensors' due to the reciprocity principle. The larger range of velocities may be due to the MFP method optimizing velocities over all source-to-station paths, while the SMI method locally optimizes the velocity thus preserving local heterogeneity.

In Figure 3c, we show the distribution of the spatial variability of the phase velocity obtained from SMI (absolute deviation to the mean) and the distribution of the velocity uncertainty. The SMI-velocities vary by up to 60 m.s^{-1} and the associated uncertainties are restricted within the [10-20] m.s^{-1} range. In Figure S4b we show the spatial distribution of the uncertainties and see that higher uncertainty occurs where the source density is lower, likely resulting from a poorly constrained fit between the data-based DKs and the theoretical interference fringes (Fig. 3a, b). No clear relationship however occurs between velocity variability and velocity uncertainty.

4 Discussion

4.1 Spatial Variations in Phase Velocity and Glacier Structure

In Figure4a, we assess the spatial resolution of the SMI phase velocity field. We first evaluate the change in phase velocities between two sources as a function of their distance Δr_s (Fig.4a, shaded area and red dots). We observe average variations in phase velocity within [0-20] $m.s^{-1}$ for short distances ([0-20] m) and above 30 $m.s^{-1}$ for larger distances (>50 m). We fit our observations with a negative exponential function (Fig.4a, green line) of the form $\Delta\phi\times(1-e^{-\Delta r_s/l})$. l represents the characteristic distance over which the phase velocity variations exhibit significant correlation and $\Delta\phi$ the plateau for phase velocity variations at large Δr_s. The best fit is obtained for a correlation length of $l = 20.3$ m (left-most blue dashed line in Fig.4a) and for a scaling factor $\Delta\phi = 33.6$ $m.s^{-1}$. The correlation length of 20m, i.e. the spatial resolution, corresponds to half of the inter-receiver distance (purple dashed-dotted line in Fig.4a) and nearly one-seventh of the wavelength (114m; half wavelength in black dotted line in Fig.4a). Such a resolution is thus notably better than that obtained in previous applications (Chmiel, Roux, et al., 2021) and with conventional methods (Gimbert, Nanni, et al., 2021). Conventional phase velocity maps are typically generated through surface wave tomography and require spatial regularization, resulting in a spatial resolution of about twice the inter-receiver distance (here c. 100 m; Fig.1), thus five times lower than presently. Such a difference makes irrelevant at small scale ($<$ 100m) the comparison between the travel-time tomography-based velocity field and the SMI-based velocity field (Fig. 3; Fig. S3). Our approach not only enables remote imaging of damaged zones but also facilitates mapping at the necessary spatial resolution to investigate rapid phase velocity changes in highly heterogeneous regions. In our setup, this resolution allows us to preserve local phase velocity heterogeneities that are otherwise hindered (Fig. S3). This enhanced resolution is particularly important as fine-scale heterogeneity likely indicates a complex 3-D medium (Preiswerk et al., 2019).

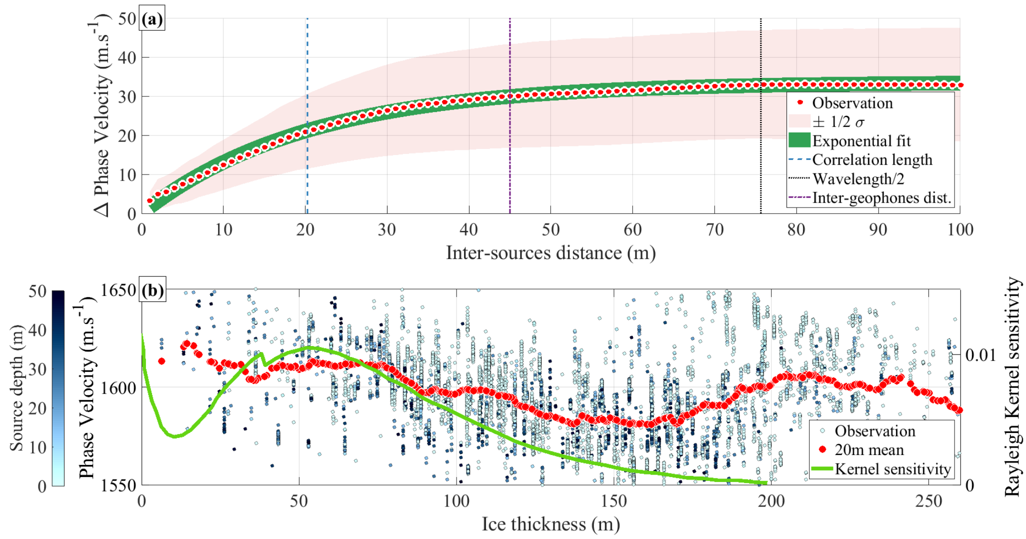

Figure 4. (a) Phase velocity variations as a function of source inter-distance averaged over N=55,266,841 source pairs ($\frac{N_{\text{source}}\times(N_{\text{source}}-1)}{2}$, red line). A function (green line) of the form $\Delta\phi\ \times\ (1\ -\ e^{-\Delta r_s/l})$ is fitted on the data (red dots), yielding a correlation length of $l\ \ = 20.3\ m$ (left-most blue dashed line) and a scaling factor $\Delta\phi\ \ = 33.6\ m.s^{-1}$. Averaged inter-receivers distance (45m, dashed dotted purple line) and the investigated wavelength (114m; half wavelength in dotted black line) are shown. (b) Phase velocity as a function of ice thickness at the source location, with source-depth color coded. Green line shows the Rayleigh Kernel Sensitivity Kernel at 11 Hz (as in Fig. 10 in Gimbert, Nanni, et al., 2021).

In Figure4b, we explore the influence of glacier geometry (ice thickness) on the variations of phase velocity. As ice thickness increases from 0 to 150 m, the phase velocity decreases from $\sim$ 1610 to $\sim$ 1580 $m.s^{-1}$. This 30 $m.s^{-1}$ change is significant as it is greater than the upper range of the phase velocity uncertainty (Fig.3c) and likely happens over distances larger than the spatial resolution (Fig.4a). Subsequently, as ice thickness increases to $\sim$ 250 m, the phase velocity rises back up to $\sim$ 1600 $m.s^{-1}$. In Figure S5 we show that this evolution does not depend on the region of investigation. We analyze this trend (Fig. 4b, red line) alongside the sensitivity kernels for fundamental mode Rayleigh waves (Fig. 4b, green line). The kernels show that the seismic waves sensitivity is more pronounced in the first 100 to 150 m below the surface and peaks at about 50m. For an ice thickness lower than 150m, seismic waves are thus likely sensitive to both the ice (phase velocity of $\sim$ 1580 m.s^{-1}) and the underlying bedrock (phase velocity larger than 2800 $m.s^{-1}$; Gimbert, Nanni, et al., 2021). We suggest that the decrease in phase velocity with ice thickness observed in the shallow parts of the glacier (up to $\sim$ 150 m thick) results from the progressively reduced sensitivity to the bedrock. For an ice thickness larger than c. 150 m (i.e., beyond the primary sensitivity area), we propose that the increase in phase velocity may be linked to reduced ice damage, possibly resulting from fewer crevasses away from the glacier's side (Fig. 3b) as the presence of crevasses tends to reduces the phase velocity (Zhan, 2019).

While the relative ice-bed sensitivity of the wavefield seems to be the primary control on phase velocity for ice thicknesses until c. 150 m, we still observe a large variability in this relationship (Fig.4c). We suggest that such a variability may be related to other structural features, such as crevasses or debris within the ice (e.g., Fig. 3 in Nanni et al., 2022). Another potential cause is the medium anisotropy that we do not resolve for here. Comparing our phase velocity map and the anisotropy map proposed by Sergeant et al. (2020, Fig. 6;), however, we do not see a clear correlation. In order to disentangle the joint influence of ice thickness and ice micro-structure on phase velocity, one could investigate phase velocity maps at different frequencies. Additionally, employing a local 1-D inversion based on surface wave dispersion curves (Gimbert, Nanni, et al., 2021) may prove inadequate in this complex 3-D medium. We rather suggest a global 3D approach, such as Full Waveform Inversion with viscoelastic modeling. This approach should incorporate local measurements of anisotropy and attenuation, particularly in glacier environments (Lindner et al., 2019; Sergeant et al., 2020).

4.2 Applicability and Perspectives

The pre-requisite of our approach is to dispose of well located and spatially spread sources close enough with each other for spatial aliasing to be avoided and Diffraction Kernels (DKs) to be properly sampled (Fig. 2). In practice, observing interference fringes relies on having at least two points per half-wavelength. This constraint is relatively challenging, as phase cycles in the DKs do not solely depend on the frequency, and vary with the receiver-source distance (Eqs. 3 and 4; Fig. S2). In our case, the number of icequakes located from Matched Field Processing satisfies the spatial aliasing criteria on large parts of the glacier surface where an accurate phase velocity inversion can be performed (Fig. 2a-b). The application of SMI is therefore particularly applicable to seismogenic environments where a network of receivers provides an accurate localization of naturally-induced seismic sources.

Previous studies, at the same location, identified additional seismic sources from subglacial water flow (Nanni, Gimbert, Roux, & Lecointre, 2021a) and from diffracting objects in the glacier's central part (Nanni et al., 2022). These tremor-like sources, operating at different frequencies, may offer supplementary insights into glacier properties. Synchronizing these sources poses a challenge since the origin time of a given tremor is challenging to define. This synchronization difficulty would affect the use of convolution for surface-wave interferometry (Eq. 1). In contrast, correlation-based DKs (Eq. 2) do not require synchronization because of phase cancellation in the correlation process. SMI computation would thus rely solely on correlation-based DKs, potentially yielding less accurate results than with impulsive sources, especially at low frequency (Chmiel et al., 2018). Yet, these additional sources, are nearly ten times more prevalent than crevasse-related icequakes (Nanni et al., 2022), potentially compensating for resolution loss through statistical significance. Given the inherent challenges in monitoring the ice-bed interface, utilizing seismic noise to perform SMI could yield valuable insights into the structural characteristics of these areas, which are crucial for understanding glacier bed friction and subglacial hydrology (Gimbert, Gilbert, et al., 2021; Gilbert et al., 2022) as well as glacier stability (Thøgersen et al., 2019).

5 Conclusions

We utilize source-to-receiver spatial reciprocity to transform well-localized seismic sources into virtual receivers. Through the calculation of phase interference patterns between these virtual receivers, we obtain a phase velocity map in otherwise inaccessible areas using Seismic Michelson Interferometry. The resulting map is derived at the seismic sources location, extending beyond the boundaries of the receiver array deployment. Notably, we observe changes in phase velocity related to ice thickness and crevasse presence with a spatial resolution five times higher than traditional methods. Looking forward, this approach will enhance our understanding of complex subsurface changes in mechanical properties in a more nuanced and comprehensive manner, particularly in areas previously considered inaccessible. Finally, we argue that our approach is neither limited to glacier environments nor to the presence of impulsive sources, therefore leaving opportunities in expanding its application to a wide variety of seismogenic environments.

6 Open Research

The codes used to localize seismic sources are described and available via `https://lecoinal.gricad-pages.univ-grenoble-alpes.fr/resolve/` (last access: 19/12/2023) under a creative commons attribution 4.0 inter- national license. The data derived from the matched-field-processing (i.e., 29 sources localizations per second over 34 days and for 20 frequency bands) together with 1 day of raw seismic signal recorded over the 98 seismic stations are available via Nanni, Gimbert, Roux, and Lecointre (2021b) under a creative commons attribution 4.0 inter- national license (Nanni et al., 2022). The complete set of raw seismic data can be found via Roux et al. (2021) under a creative commons attribution 4.0 international license. The complementary data associated with the dense array experiment, including the actives crevasses identification, are available via Nanni, Gimbert, and RESIF (2021) under a creative commons attribution 4.0 international license (Gimbert, Nanni, et al., 2021).

Acknowledgments

The authors declare no financial conflict of interest. This work has been conducted in the framework of the RESOLVE Project (`https://resolve.osug.fr/`; LabEx OSUG@2020, Investissement d'avenir – ANR10LABX56 and IDEX Université Grenoble Alpes).

UN has received support from the Research Council of Norway through the projects MAMMAMIA (grant no. 301837) and SLIDE (no. 337228) and acknowledge support from Circle U. 2023 seed-funding scheme. FG acknowledges support from ANR SEISMORIV (ANR-17-CE01-0008) and SAUSSURE (ANR-18-CE01-0015-01). We thank two anonymous reviewers and the Editor Matthieu Morlighem for their constructive comments that improved the paper.

PR designed the study. UN and PR conducted the study, processed the seismic data and wrote the first draft. FG contributed to refinements of the interpretations and editing of the manuscript.

References

Chandler, D. M., & Hubbard, A. (2023). Widespread partial-depth hydrofractures in ice sheets driven by supraglacial streams. *Nature Geoscience*, 1–7.

Chmiel, M., Roux, P., Herrmann, P., Rondeleux, B., & Wathelet, M. (2018). Data-based diffraction kernels for surface waves from convolution and correlation processes through active seismic interferometry. *Geophysical Journal International*, *214*(2), 1468–1480.

Chmiel, M., Roux, P., Wathelet, M., & Bardainne, T. (2021). Phase-velocity inversion from data-based diffraction kernels: seismic michelson interferometer. *Geophysical Journal International*, *224*(2), 1287–1300.

Chmiel, M., Walter, F., Wenner, M., Zhang, Z., McArdell, B. W., & Hibert, C. (2021). Machine learning improves debris flow warning. *Geophysical Research Letters*, *48*(3), e2020GL090874.

Curtis, A. (2009). Source-receiver seismic interferometry. In *Seg international exposition and annual meeting* (pp. SEG–2009).

Curtis, A., Gerstoft, P., Sato, H., Snieder, R., & Wapenaar, K. (2006). Seismic interferometry—turning noise into signal. *The Leading Edge*, *25*(9), 1082–1092.

Fichtner, A., Stehly, L., Ermert, L., & Boehm, C. (2016). Generalised interferometry-i. theory for inter-station correlations. *Geophysical Journal International*, ggw420.

Fichtner, A., Tsai, V., Nakata, N., & Gualtieri, L. (2019). Theoretical foundations of noise interferometry. *Seismic ambient noise*, 109–143.

Gagliardini, O., & Werder, M. A. (2018). Influence of increasing surface melt over decadal timescales on land-terminating greenland-type outlet glaciers. *Journal of Glaciology*, *64*(247), 700–710.

Gilbert, A., Gimbert, F., Thøgersen, K., Schuler, T. V., & Kääb, A. (2022). A consistent framework for coupling basal friction with subglacial hydrology on hard-bedded glaciers. *Geophysical Research Letters*, *49*(13), e2021GL097507.

Gilbert, A., Sinisalo, A., Gurung, T. R., Fujita, K., Maharjan, S. B., Sherpa, T. C., & Fukuda, T. (2020). The influence of water percolation through crevasses on the thermal regime of a himalayan mountain glacier. *The Cryosphere*, *14*(4), 1273–1288.

Gimbert, F., Gilbert, A., Gagliardini, O., Vincent, C., & Moreau, L. (2021). Do existing theories explain seasonal to multi-decadal changes in glacier basal sliding speed? *Geophysical Research Letters*, *48*(15), e2021GL092858.

Gimbert, F., Nanni, U., Roux, P., Helmstetter, A., Garambois, S., Lecointre, A., ... others (2021). A multi-physics experiment with a temporary dense seismic array on the argentière glacier, french alps: The resolve project. *Seismological Research Letters*, *92*(2A), 1185–1201.

Guest, P., & Clouston, J. (1950). Fresnel interference in the michelson interferometer. *JOSA*, *40*(11), 787–787.
Hernigou, P. (2022). History of bone acoustic in fracture diagnosis: crepitus in antiquity; bone percussion with auenbrugger; bone auscultation with laennec and lisfranc; monitoring cementless hip arthroplasty fixation with acoustic and sensor. *International Orthopaedics*, *46*(7), 1657–1666.
Knopoff, L., & Gangi, A. F. (1959). Seismic reciprocity. *Geophysics*, *24*(4), 681–691.
Lhermitte, S., Sun, S., Shuman, C., Wouters, B., Pattyn, F., Wuite, J., ... Nagler, T. (2020). Damage accelerates ice shelf instability and mass loss in amundsen sea embayment. *Proceedings of the National Academy of Sciences*, *117*(40), 24735–24741.
Lin, F.-C., Ritzwoller, M. H., & Snieder, R. (2009). Eikonal tomography: surface wave tomography by phase front tracking across a regional broad-band seismic array. *Geophysical Journal International*, *177*(3), 1091–1110.
Lindner, F., Laske, G., Walter, F., & Doran, A. K. (2019). Crevasse-induced rayleigh-wave azimuthal anisotropy on glacier de la plaine morte, switzerland. *Annals of Glaciology*, *60*(79), 96–111.
Lobkis, O. I., & Weaver, R. L. (2001). On the emergence of the green's function in the correlations of a diffuse field. *The Journal of the Acoustical Society of America*, *110*(6), 3011–3017.
Marty, S., Passelègue, F., Aubry, J., Bhat, H., Schubnel, A., & Madariaga, R. (2019). Origin of high-frequency radiation during laboratory earthquakes. *Geophysical Research Letters*, *46*(7), 3755–3763.
Métivier, L., Brossier, R., Virieux, J., & Operto, S. (2013). Full waveform inversion and the truncated newton method. *SIAM Journal on Scientific Computing*, *35*(2), B401–B437.
Mordret, A., Mikesell, T. D., Harig, C., Lipovsky, B. P., & Prieto, G. A. (2016). Monitoring southwest greenland's ice sheet melt with ambient seismic noise. *Science advances*, *2*(5), e1501538.
Nanni, U., Gimbert, F., & RESIF. (2021). *Data of the resolve project [dataset] (version v0).* `https://resolve.osug.fr/`. RESIF - Réseau Sismologique et géodésique Français. doi: 10.5281/ZENODO.3971815
Nanni, U., Gimbert, F., Roux, P., & Lecointre, A. (2021a). Observing the subglacial hydrology network and its dynamics with a dense seismic array. *Proceedings of the National Academy of Sciences*, *118*(28), e2023757118.
Nanni, U., Gimbert, F., Roux, P., & Lecointre, A. (2021b). *Seismic source location with a match field processing approach during the resolve dense seismic array experiment on the glacier d'argentiere [dataset].* `http://doi.org/10.5281/ZENODO.5645545`. Zenodo. doi: 10.5281/ZENODO.5645545
Nanni, U., Roux, P., Gimbert, F., & Lecointre, A. (2022). Dynamic imaging of glacier structures at high-resolution using source localization with a dense seismic array. *Geophysical Research Letters*, *49*(6), e2021GL095996.
Preiswerk, L. E., Michel, C., Walter, F., & Fäh, D. (2019). Effects of geometry on the seismic wavefield of alpine glaciers. *Annals of Glaciology*, *60*(79), 112–124.
Pyrak-Nolte, L. J., de Pater, C., & Jocker, J. (2005). Seismic monitoring of fracture formation. In *Arma us rock mechanics/geomechanics symposium* (pp. ARMA–05).
Roux, P., Gimbert, F., & RESIF. (2021). *Dense nodal seismic array temporary experiment on alpine glacier of argentière (resif-sismob) [dataset].* `http://doi.org/10.15778/RESIF.ZO2018`. RESIF - Réseau Sismologique et géodésique Français. doi: 10.15778/RESIF.ZO2018
Roux, P., Kuperman, W., & group, N. (2004). Extracting coherent wave fronts from acoustic ambient noise in the ocean. *The Journal of the Acoustical Society of America*, *116*(4), 1995–2003.

Schuster, R. L., & Rigsby, G. P. (1954). Preliminary report on crevasses. -.

Sergeant, A., Chmiel, M., Lindner, F., Walter, F., Roux, P., Chaput, J., ... Mordret, A. (2020). On the green's function emergence from interferometry of seismic wave fields generated in high-melt glaciers: implications for passive imaging and monitoring. *The Cryosphere*, *14*(3), 1139–1171.

Shankland, R. S. (1974). Michelson and his interferometer. *Physics Today*, *27*(4), 37–43.

Shapiro, N. M., Campillo, M., Stehly, L., & Ritzwoller, M. H. (2005). High-resolution surface-wave tomography from ambient seismic noise. *Science*, *307*(5715), 1615–1618.

Share, P.-E., Allam, A. A., Ben-Zion, Y., Lin, F.-C., & Vernon, F. L. (2019). Structural properties of the san jacinto fault zone at blackburn saddle from seismic data of a dense linear array. *Pure and Applied Geophysics*, *176*, 1169–1191.

Snieder, R. (2004). Extracting the green's function from the correlation of coda waves: A derivation based on stationary phase. *Physical review E*, *69*(4), 046610.

Taylor, C., Robinson, T. R., Dunning, S., Rachel Carr, J., & Westoby, M. (2023). Glacial lake outburst floods threaten millions globally. *Nature Communications*, *14*(1), 487.

Thøgersen, K., Gilbert, A., Schuler, T. V., & Malthe-Sørenssen, A. (2019). Rate-and-state friction explains glacier surge propagation. *Nature communications*, *10*(1), 2823.

Van der Veen, C. (1998). Fracture mechanics approach to penetration of surface crevasses on glaciers. *Cold Regions Science and Technology*, *27*(1), 31–47.

Virieux, J., Asnaashari, A., Brossier, R., Métivier, L., Ribodetti, A., & Zhou, W. (2017). An introduction to full waveform inversion. In *Encyclopedia of exploration geophysics* (pp. R1–1). Society of Exploration Geophysicists.

Walker, S. (2012). Coherence and interference in diffuse noise: On the information and statistics associated with spatial wave correlations in directional noise fields. *The Journal of the Acoustical Society of America*, *131*(3), 1987–1998.

Walter, J. I., Svetlizky, I., Fineberg, J., Brodsky, E. E., Tulaczyk, S., Barcheck, C. G., & Carter, S. P. (2015). Rupture speed dependence on initial stress profiles: Insights from glacier and laboratory stick-slip. *Earth and Planetary Science Letters*, *411*, 112–120.

Xu, Z., Juhlin, C., Gudmundsson, O., Zhang, F., Yang, C., Kashubin, A., & Lüth, S. (2012). Reconstruction of subsurface structure from ambient seismic noise: an example from ketzin, germany. *Geophysical Journal International*, *189*(2), 1085–1102.

Yoshizawa, K., & Kennett, B. (2002). Determination of the influence zone for surface wave paths. *Geophysical Journal International*, *149*(2), 440–453.

Zhan, Z. (2019). Seismic noise interferometry reveals transverse drainage configuration beneath the surging bering glacier. *Geophysical Research Letters*, *46*(9), 4747–4756.